

# Magnetic properties of carbon nanodisk and nanocone powders

Jozef Černák

*Institute of Physics, P. J. Šafárik University in Košice,  
Jesenná 5, SK-04000 Košice, Slovak Republic*

Geir Helgesen and Arne T. Skjeltorp

*Institute for Energy Technology, Physics Department, NO-2007 Kjeller, Norway*

Jozef Kováč

*Laboratory of nanomaterials and applied magnetisms,  
Institute of Physics, Slovak Academy of Sciences,  
Watsonova 47, SK-04000 Košice, Slovak Republic*

Josef Voltr

*Faculty of Nuclear Sciences and Physical Engineering,  
Czech Technical University in Prague,  
Břehová 7, CZ-115 19 Praha 1, Czech Republic*

Erik Čížmár

*Centre of Low Temperature Physics,  
P. J. Šafárik University in Košice, SK-04000 Košice, Slovak Republic*

## Abstract

We have investigated the magnetic properties of carbon powders which consist of nanodisks, nanocones, and a small fraction of carbon-black particles. Magnetization measurements were carried out using a superconducting quantum interference device in magnetic fields  $-5 < \mu_0 H < 5$  T for temperatures in the range  $2 \leq T < 350$  K. Measurements of the magnetization  $M$  versus temperature  $T$  and magnetic field  $\mu_0 H$  for these carbon samples show diamagnetism and paramagnetism with an additional ferromagnetic contribution. The ferromagnetic magnetization is in agreement with the calculated magnetization from Fe impurities as determined by the particle-induced x-ray emission method ( $< 75 \mu\text{g/g}$ ). Magnetization measurements in weak magnetic fields show thermal hysteresis, and for strong fields the magnetization  $M$  decreases as  $M \sim aT^{-\alpha}$  with  $\alpha < 1$ , which is slower than the Curie law ( $\alpha = 1$ ), when the temperature increases. The magnetization  $M$  versus magnetic field  $\mu_0 H$  shows paramagnetic free-spin  $S = \frac{1}{2}$  and  $\frac{3}{2}$  behaviors for temperatures  $T = 2$  K and  $15 \leq T \leq 50$  K, respectively. A tendency for localization of electrons was found by electron spin resonance when the temperature  $T$  decreases ( $2 < T < 40$  K). The magnetic properties in these carbon cone and disk powder samples are more complex than a free-spin model predicts, which is apparently valid only for the temperature  $T = 2$  K.

## I. INTRODUCTION

Carbon atoms can bind via  $\sigma$  and  $\pi$  bonds when forming a molecule. The number and nature of the bonds determine the geometry and properties of carbon allotropes.<sup>1</sup> Elemental carbon naturally forms three well-known allotropes: graphite, diamond, and carbon black. In the past, new carbon allotropes have been synthesized: fullerenes, carbon nanotubes,<sup>2</sup> and graphene.<sup>3</sup> Two recently published papers<sup>2,4</sup> illustrate an effort to propose and design new carbon allotropes. The structure of carbon nanocones<sup>5</sup> containing a small number of pentagons in a graphene-like layer of hexagons is the reason why nanocones often have been considered to be a specific kind of fullerene.<sup>6</sup> However, the nanocones and nanodisks differ from fullerenes in shape<sup>5</sup> and wall thickness which may be from a few up to several tens of graphene layers. These differences could be a reason for their different properties relative to the fullerenes.

Elemental-carbon-based materials show a diversity of electronic properties metallic, semi-conducting, or dielectric,<sup>3</sup> but they are commonly classified as semiconductors.<sup>7</sup> For example, a single graphene layer or stack of a few graphene layers can display Dirac-like electron excitations which result in unusual spectroscopic and transport properties.<sup>3</sup> The magnetic properties of graphite are diamagnetic due to the delocalized  $\pi$ -band electrons. On the other hand, diamond displays paramagnetic magnetization as a consequence of localized electrons. Flow of currents around the carbon rings of graphite in response to an applied magnetic field has been used to explain the differences between the susceptibility of graphite and that of diamond found in experiments.<sup>8</sup> The fullerenes can exhibit both diamagnetic and paramagnetic ring currents which lead to subtle effects in the magnetic properties of these molecules and provide evidence for the existence of  $\pi$  electrons mobile in three dimensions.<sup>8</sup>

The early reports on possible ferromagneticlike behavior in carbon structures were not generally accepted by the scientific community.<sup>9</sup> It was initially assumed that ferromagnetic behavior results from residual amounts of ferromagnetic impurities (Fe, Ni, or Co) in the carbon samples. A systematic study performed by Hohne *et al.*<sup>10</sup> did not show any influence of iron atoms on the ferromagnetic properties of highly oriented pyrolytic graphite (HOPG) up to Fe impurity densities of  $\sim 4000 \mu\text{g/g}$ , and this supported the initial assumption that uniformly distributed iron up to 100 ppm cannot trigger ferromagnetic order.<sup>7</sup> The reason is that uniformly distributed residual magnetic impurities can be considered to be

noninteracting magnetic moments.<sup>11</sup> However, recently Nair *et al.*<sup>12</sup> found Fe microparticles which were attached to the surface of HOPG samples. These bigger Fe microparticles behave in a quite different manner from uniformly distributed Fe nanoparticles and could contribute in a ferromagnetic way to the sample magnetization.

Carbon nanofoams<sup>13</sup> and nanodiamond powders<sup>14</sup> have the common feature that their magnetizations  $M$  vs temperature  $T$  show paramagnetic behavior in a wide temperature range. However, the reasons for their paramagnetism are different. The paramagnetic behavior of the carbon nanofoams<sup>13</sup> is considered to be a consequence of a metal-insulator-like transition which can take place<sup>15</sup> for temperatures  $T < 30\text{K}$ . In the case of nanodiamond powder,<sup>14</sup> the paramagnetic magnetization is associated with localized electrons in a wide temperature range. Sepioni *et al.*<sup>16</sup> have investigated graphene nanocrystals of size 10 to 50 nm and thickness of one or two graphene layers. They observed a strong diamagnetic behavior and found only a weak paramagnetism caused by unpaired electrons at edges for low temperatures  $2 \leq T \leq 50\text{K}$ . Spemann *et al.*<sup>17</sup> reported on the ferromagnetic behavior of impurity-free regions of a  $\text{C}_{60}$  polymer. For the Rh –  $\text{C}_{60}$  polymerized phase, Boukhvalov *et al.*<sup>18</sup> concluded that rhombohedral distortion of  $\text{C}_{60}$  itself cannot induce magnetic ordering in molecular carbon. Červenka *et al.*,<sup>19</sup> using superconducting quantum interference device (SQUID) magnetization measurements at temperatures  $T = 5$  and 300 K and scanning tunneling microscopy (STM), demonstrated both diamagnetism and ferromagnetic order at room temperatures in bulk HOPG caused by two-dimensional (2D) planes of magnetized grain boundaries propagating through the sample. However, the existence of ferromagnetic order in bulk HOPG samples is not conclusively confirmed.<sup>12,20</sup>

González *et al.*<sup>21</sup> theoretically investigated electron-electron interaction in graphene layers. They found that topological disorder enhances the density of states and can lead to instabilities in conductivity or magnetic properties. Park *et al.*<sup>22</sup> applied *ab initio* spin density functional theory to demonstrate a net magnetic moment in the building block of schwarzite. They expected that in aromatic systems with negative Gaussian curvature unpaired spins can be introduced by sterically protected carbon radicals. The magnetic moment of a vacancy defect has been determined as  $1.12 - 1.53 \mu_B$  (Bohr magneton) from first-principle calculations.<sup>23</sup> Experimental<sup>24,25</sup> and theoretical results<sup>21-23</sup> support the hypothesis that disorder in carbon allotropes is an important precondition in order to observe paramagnetic or ferromagnetic magnetization.

The aim of this paper is to characterize the basic magnetic properties of a carbon powder consisting of nanocones and nanodisks and discuss its magnetic properties in comparison to other carbon allotropes.

The paper is organized as follows. In the next section, Sec. II, the carbon powder samples and the experimental methods are described. The results of magnetic measurements are presented in Sec. III and discussed in Sec. IV. Conclusions are given in Sec. V.

## II. EXPERIMENTS

### A. Carbon powder samples

The graphitic carbon powder was produced by the so-called pyrolytic Kvaerner “carbon-black and hydrogen process”<sup>26</sup>. The powder consists of flat carbon nanodisks, open-ended carbon cones, and a smaller amount of carbon black.<sup>5,27,28</sup>

The carbon disks and cones exhibit a wide range of diameters (500 – 4000 nm) and their wall thickness is mainly 10 – 30 nm but particles with thickness in the range 5 – 70 nm can be found. The electron diffraction patterns of the nanodisks consist of concentric continuous rings with distinct spots with six-fold rotational symmetry. These results led to the conclusion that the nanodisks are multilayer carbon structures with a graphitic core and outer non-crystalline layers,<sup>28</sup> which was also supported by scanning electron microscopy (SEM) and transmission electron microscopy (TEM) images. TEM micrographs of the carbon powder showed the presence of perfect carbon nanocones of all the five possible apex angles<sup>5</sup>  $\alpha = 112.9^\circ$ ,  $83.6^\circ$ ,  $60.0^\circ$ ,  $38.9^\circ$ , and  $19.2^\circ$  corresponding to  $n = 1 - 5$  carbon pentagonal rings near the cone tip.  $n = 0$  corresponds to the flat disks. Later, electron diffraction analysis of the nanocones showed that they are similar to the disks with a graphitic core surrounded by amorphous outer carbon layers.<sup>29</sup> Some of the disks and the  $112.9^\circ$  apex-angle cones showed six-fold and five-fold faceting, respectively, along their edges. The thickness of the crystalline core was estimated to be only 10 – 30% of the disk thickness. These cones are different from the conical graphite crystals reported by Gogotsi *et al.*<sup>30</sup> and carbon nanohorns.<sup>31</sup>

The investigated sample shows disorder on at least two length scales; on the nanometer scale it is a mixture of crystalline parts, possibly containing many dislocations, grain bound-

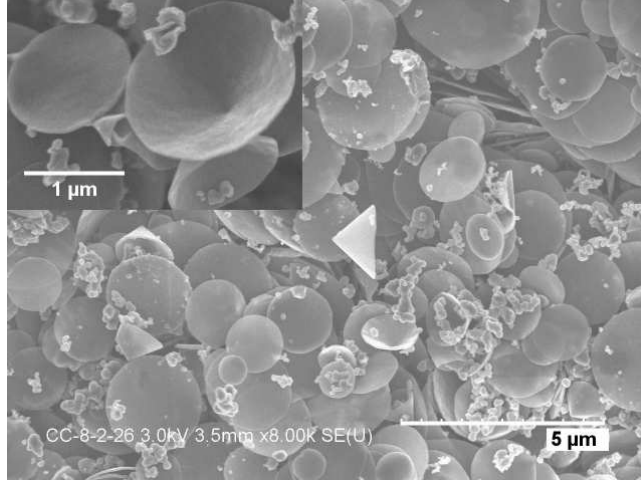


FIG. 1: Scanning electron microscopy micrographs of the carbon powder. The inset shows details of the cones.

aries, and other defects, and non-crystalline or amorphous matter. On the micrometer scale the grainy nature of the powder will cause different packings of particles and thus a varying material density.

## B. Experimental methods

### 1. Iron impurity measurements

It is quite common that carbon nanomaterials contain trace amounts of Fe contamination. Therefore, it is important to determine the density of magnetic impurities such as Fe in the carbon powder. Here, the particle induced x-ray emission method<sup>32</sup> was used to determine the Fe content. The carbon powder was fixed on polycarbonate membranes of diameter 25 mm with pore size of 5  $\mu\text{m}$  (Cyclopore). In order to determine the mass of powder, the difference between membrane mass without powder and with powder after deposition was determined. The mass of powder was in the range 0.1 – 0.2 mg (using a Mettler Toledo balance). Taking into account the density of amorphous carbon  $\sim 2300 \text{ kg}^{-3}$ , the thickness of the deposit was in the range 2 – 4  $\mu\text{m}$ . A spot of diameter 5 mm was irradiated by a proton beam of energy 1.8 MeV from a Van de Graaff accelerator at the ion beam facilities at the Czech Technical University. The diameter of the ion beam was 8 mm. Samples were placed perpendicular to the beam axis and a Si(Li) detector was used to collect x-rays at

an angle of  $60^\circ$ . In order to attenuate the low- energy part of the spectra, a Mylar foil of  $356\ \mu\text{m}$  thickness was placed in front of the detector. Beam doses of  $15 - 30\ \mu\text{C}$  were measured using a Faraday cup behind the sample. A thin standard of Fe (MicroMatter) was used to obtain the reference energy spectra of Fe. Energy spectra were calculated by the GUPIXWIN software package,<sup>33</sup> where background spectra of the polycarbonate membrane were subtracted. The mass of Fe was related to the mass of carbon material. The powder samples were analyzed after magnetization measurements in order to determine the possible Fe contamination during sample handling and manipulation. Fe concentrations of about  $60\pm 15\ \mu\text{g/g}$  were found for several of these powder samples.

### 2. *Electron spin resonance*

In order to determine possible deviations from the normal electron spin g-factor electron spin resonance (ESR) measurements were performed. These were done using a Bruker ELEXSYS E500 X-band spectrometer working in the temperature range  $2 - 300\ \text{K}$  on powder samples mixed with Apiezon-N grease and attached to a Suprasil sample holder.

### 3. *Magnetization measurements*

Magnetization vs temperature  $M(T)$  and magnetization vs magnetic field  $M(\mu_0 H)$  measurements were carried out using a Quantum Design dc-ac SQUID magnetic properties measurement system (MPMS) magnetometer with a scan length of  $4\ \text{cm}$ . The samples were placed in the SQUID chamber before magnetization measurements for  $4\ \text{h}$  to reduce the concentration of oxygen in the sample. The pressure of helium gas near the sample in the SQUID chamber was about  $666\ \text{Pa}$ . Zero-field-cooled (ZFC) and field-cooled (FC) protocols were used to measure the temperature dependence of the magnetization. During ZFC the samples were cooled to  $2\ \text{K}$  in zero field. Once the temperature was stabilized, the magnetic field was applied. The magnetic moment was measured as a function of temperature up to room temperature  $T = 300\ \text{K}$ . For FC the samples were cooled in the same constant field to the lowest temperature  $T = 2\ \text{K}$  and magnetization  $M(T)$  was measured.

Magnetization vs magnetic field  $M(\mu_0 H)$  was measured for a few, selected temperatures in the range  $2 \leq T \leq 300\ \text{K}$  in a varying magnetic field  $-5 \leq \mu_0 H \leq 5\ \text{T}$ . Several carbon

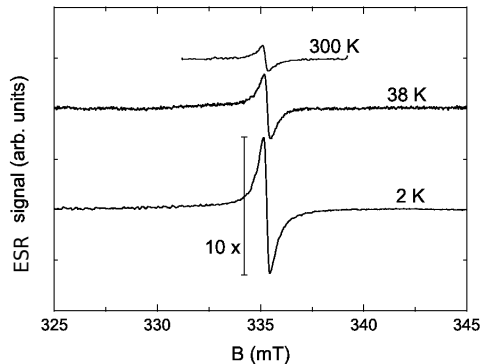


FIG. 2: Typical X-band ESR spectra of powdered sample measured at 9.4 GHz at temperatures  $T = 2, 38,$  and  $300$  K. The signal measured at 2 K is ten times reduced.

powder samples of mass  $m = 30 - 70$  mg were encapsulated in gelatin capsules of volume 0.13 ml and measured in order to check the reproducibility of the results. Here, the results of the study of a sample of mass  $m = 50$  mg will be presented. We have assumed that the density of the powder in the capsule is high enough to prevent free rotation of carbon particles caused by the magnetic field at any of the investigated temperatures. However, nano-scale movements of particles limited by surrounding particles cannot be excluded.

### III. RESULTS

#### A. ESR

The X-band ESR spectra of carbon powder measured at temperatures  $T = 2, 38,$  and  $300$  K are shown in Fig. 2. The intensity of the signal decreases significantly in the temperature range from 2 to 40 K following the temperature dependence of the magnetization (Sec. III B). A slight asymmetry of the ESR line at temperatures above 40 K was observed, reminiscent of a metallic distortion due to the skin effect, while at lower temperatures  $T < 40$  K the line is symmetric. We determined the  $g$ -factor to be  $g = 2.0026$  at 300 K; upon cooling down the  $g$  factor changes to  $g = 2.0025$  at 2 K, both close to the free electron value.

## B. Measurements of magnetization vs temperature

The temperature dependence of the zero-field-cooled and field-cooled magnetizations,  $M_{ZFC}$  and  $M_{FC}$  respectively, are shown in Fig. 3 for external magnetic fields  $\mu_0 H = 0.005, 0.1,$  and  $4$  T after subtraction of the diamagnetic background  $M_D$ . For low magnetic fields  $\mu_0 H = 0.005$  and  $0.1$  T [Figs. 3(a) and 3(b)], the magnetization curves show irreversible behavior and a strongly increasing magnetization for temperatures  $2 \leq T < 20$  K. This irreversible property tends to disappear when measurements are performed in higher magnetic fields, for example  $\mu_0 H = 4$  T as in Fig. 3 (c). For magnetic fields  $\mu_0 H > 10$  mT, the diamagnetic signal begins to be comparable to the rest of the magnetization of the sample, which results in a decrease in the total measured positive magnetization signal, and at high fields the diamagnetism dominates the measured sample response. Using a diamagnetic susceptibility  $\chi_D = -17 \times 10^{-9} \text{ m}^3\text{kg}^{-1}$  (see next section), the diamagnetic magnetizations  $M_D = -0.0014$  and  $-0.056 \text{ m}^2\text{kg}^{-1}$  were subtracted in order to get the net magnetizations from the measured  $M_{ZFC}$  and  $M_{FC}$  curves for the magnetic fields  $\mu_0 H = 0.1$  and  $4$  T, respectively.

The insets of Figs. 3(a) and 3(b) show the calculated inverse dc susceptibilities  $\chi^{-1} = H/M$  vs temperature  $T$ . For low magnetic fields  $\mu_0 H = 0.005$  and  $0.1$  T and low temperatures  $T < 20$  K [Fig. 3 (a) and 3(b)], the susceptibility does not show Curie-law-like behavior  $\chi \propto T^{-1}$ . For the highest magnetic field  $\mu_0 H = 4$  T and temperature  $2 \leq T \leq 100$  K, we found that the magnetization curve  $M(T)$  could be fitted to a temperature variable plus constant parts which were approximated by a function  $M(T) = aT^{-\alpha} + b$ , where  $a = 0.104 \pm 0.003 \text{ Am}^2\text{kg}^{-1}$ ,  $\alpha = 0.41 \pm 0.03$ , and  $b = 9.8 \times 10^{-5} \text{ Am}^2\text{kg}^{-1}$  were determined for magnetic field  $\mu_0 H = 4$  T.

## C. Magnetization vs magnetic field

Measurements of magnetization  $M$  vs magnetic field  $\mu_0 H$  for both increasing and decreasing field were performed to obtain the full magnetization loops for several temperatures in the range  $2 \leq T \leq 300$  K.

The experimental isothermal magnetization loops are shown in Fig. 4. The total magnetization  $M_E$  consists of a contributions from the diamagnetic magnetization  $M_D = -\chi_D H$ ,

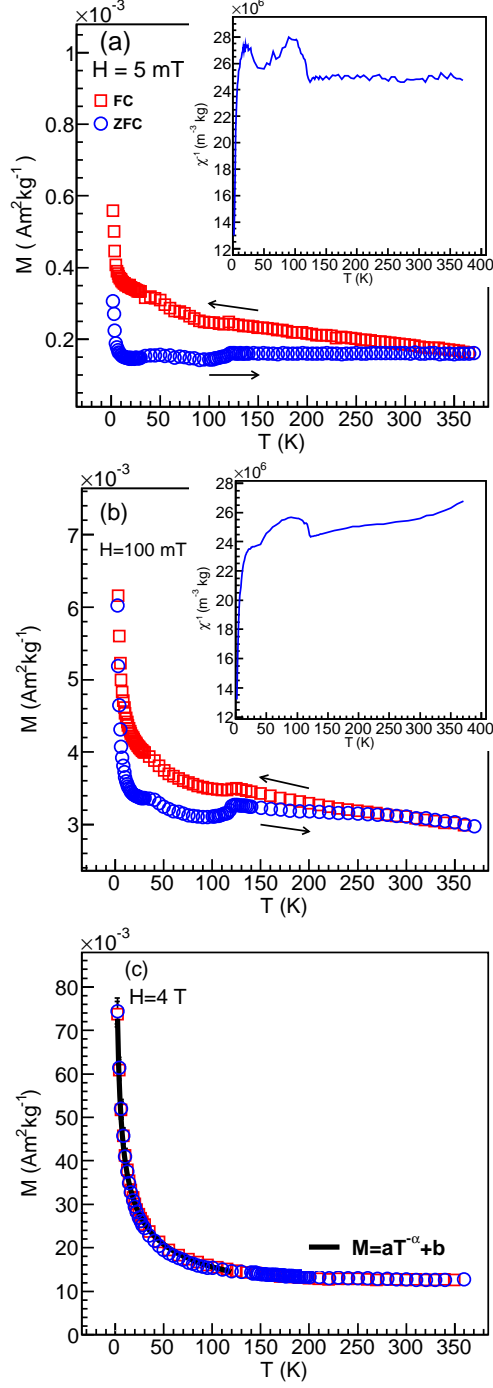


FIG. 3: (Color online) Zero-field-cooled (ZFC) and Field-cooled (FC) magnetizations at magnetic fields: (a)  $H = 5 \text{ mT}$  with diamagnetic magnetization correction  $M_D = 0 \text{ Am}^2\text{kg}^{-1}$ , (b)  $H = 100 \text{ mT}$  with diamagnetic correction  $M_D = -0.0014 \text{ Am}^2\text{kg}^{-1}$ , and (c)  $H = 4 \text{ T}$  with diamagnetic correction  $M_D = -0.056 \text{ Am}^2\text{kg}^{-1}$ . The magnetization vs. temperature  $M(T)$  is approximated by the function  $M(T) = aT^{-\alpha} + b$  where the exponent  $\alpha = 0.41 \pm 0.03$  was found for temperature  $2 \leq T \leq 100 \text{ K}$  as shown by the solid line.

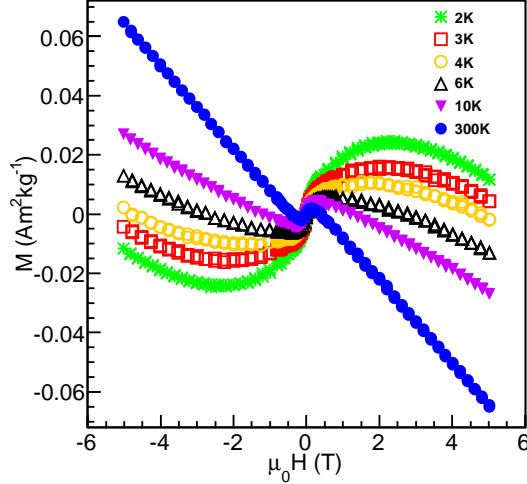


FIG. 4: (Color online) Magnetization  $M_E$  vs magnetic field  $\mu_0 H$  for temperatures  $2 \leq T \leq 300$  K.

a ferromagnetic part  $M_F$ , and an additional magnetization signal  $M$  with positive, paramagnetic sign. As the diamagnetic magnetization  $M_D$  varies linearly with the magnetic field and the ferromagnetic magnetization  $M_F(\mu_0 H)$  is known from the mainly ferromagnetic signal at ambient temperature, these components can be subtracted in order to obtain the net magnetization  $M = M_E - M_D - M_F$ . The diamagnetic contribution was determined as follows: A selection was made of the linear parts of the magnetization curves  $M_E$  vs magnetic field  $\mu_0 H$  for the temperature  $T = 300$  K and for the strongest positive and negative magnetic fields,  $4.5 \leq \mu_0 H \leq 5.0$  T and  $-4.5 \leq \mu_0 H \leq -5.0$  T. The diamagnetic susceptibility  $\chi_D = -17 \times 10^{-9} \pm 0.2 \times 10^{-9} \text{ m}^3 \text{ kg}^{-1}$  at the temperature  $T = 300$  K was then determined by fitting these two parts to one linear field behavior.

The ferromagnetic contribution  $M_F$  to the total magnetization  $M_E$  is approximately independent of the temperature in the range  $15 \leq T \leq 300$  K. The experimental isothermal magnetization loop  $M_F$  at  $T = 300$  K was well modeled by the Brillouin function Eq. (1) where the free fitting parameters were  $T = 1.34$  K,  $g = 2.0$ ,  $S = 17$ , and  $M_S = 6.3 \times 10^{-3} \text{ Am}^2 \text{ kg}^{-1}$  as shown in Fig. 5. Coercivity fields  $H_C = 20$  and  $10$  mT were found at temperatures 2 and 300 K, respectively. This ferromagnetic contribution is consistent with the Fe impurity level found in the samples (see Sec. V).

The diamagnetic magnetizations  $M_D = -\chi_D H$  and isothermal magnetization  $M_{F,T=300\text{K}}$  were subtracted from the experimentally measured magnetization values  $M_E$  in Fig. 4. The resultant magnetization curves  $M(\mu_0 H)$  are shown in Fig. 6.

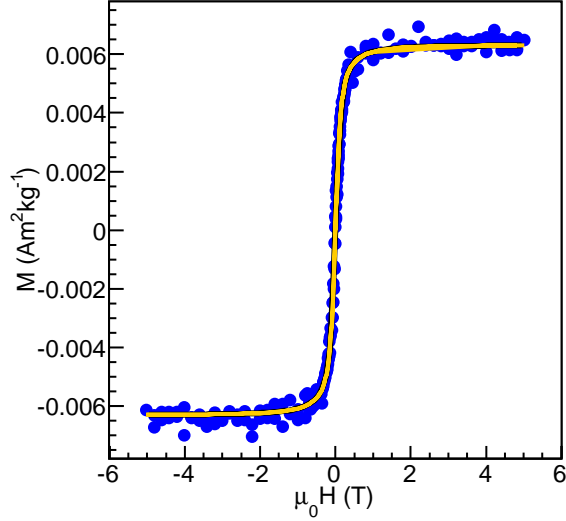


FIG. 5: (Color online) Magnetization  $M_F$  vs magnetic field  $\mu_0 H$  for temperature  $T = 300$  K. The experimental data are approximated by the Brillouin function Eq. (1).

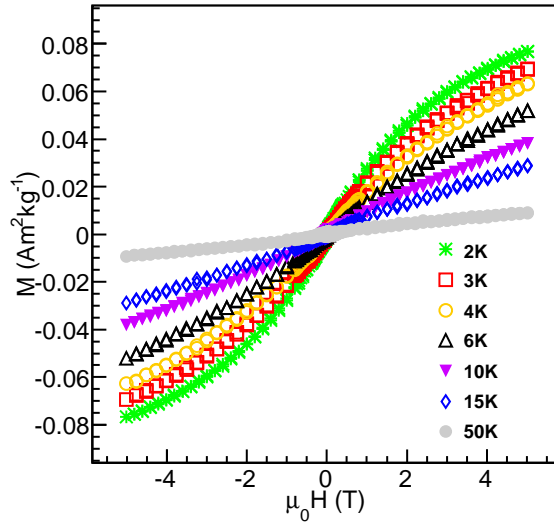


FIG. 6: (Color online) Magnetization  $M$  vs temperature  $T$  after correction of diamagnetic ( $\chi_D = -17 \times 10^{-9} \text{m}^3 \text{kg}^{-1}$ ) and ferromagnetic magnetization  $M_{F,T=300\text{K}}$  contributions.

The field dependence of the magnetization in Fig. 6 may resemble the magnetization of free, noninteracting spins. The paramagnetic magnetization of a free-spin system is described by the Brillouin function and is based on the assumption that the population of energy levels obeys Boltzmann statistics<sup>34</sup>. The rescaled magnetization, i.e., the magnetization relative to its saturation value  $M_S$ , is then  $M/M_S = B_S(x)$ . Here, the Brillouin function  $B_S(x)$  is

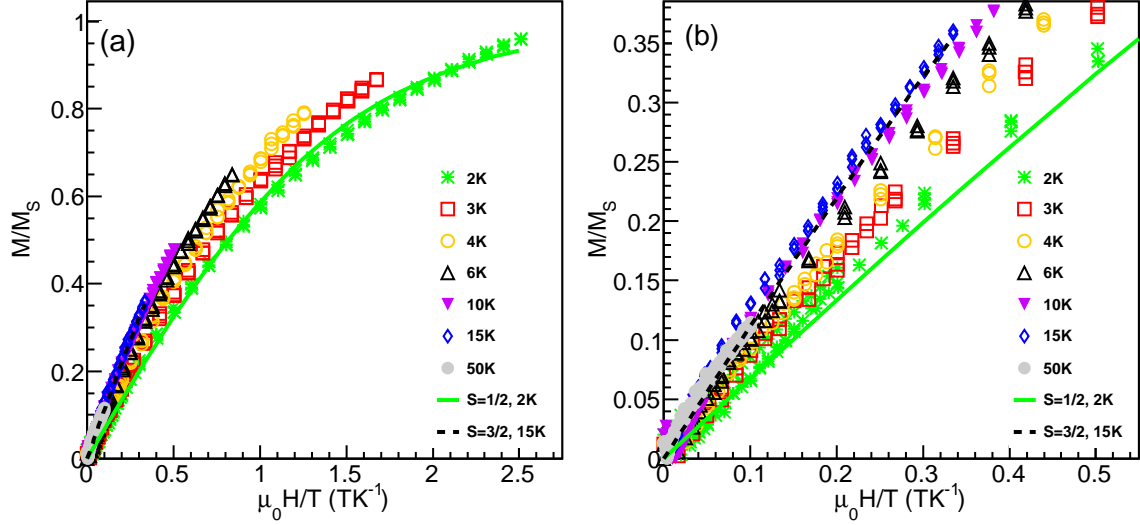


FIG. 7: (Color online) (a)  $M/M_S$  vs  $\mu_0 H/T$  plots for low temperatures  $2 \leq T \leq 50$  K. The data are fitted to Brillouin functions Eq. (1) with parameters  $g = 2.0$ ,  $S = \frac{1}{2}$  for  $T = 2$  K (solid line), and  $g = 2.0$ ,  $S = \frac{3}{2}$  for  $T = 15$  K (dashed line). (b) Magnification of the lower left-hand corner of (a).

given by

$$B_S(x) = \frac{2S+1}{2S} \coth\left(\frac{2S+1}{2S}x\right) - \frac{1}{2S} \coth\left(\frac{1}{2S}x\right) \quad (1)$$

with  $x = g\mu_B\mu_0 HS/k_B T$ , where  $S$  is the spin value,  $g$  is the Landé factor,  $\mu_B$  is the Bohr magneton,  $\mu_0$  is the permeability of vacuum, and  $k_B$  is the Boltzmann constant. The saturation magnetization is  $M_S = Ng\mu_B S$ , where  $N$  is the number of magnetic moments per unit volume. For the specific case  $S = 1/2$  Eq. (1) transforms into the hyperbolic tangent,  $B_{1/2}(x) = \tanh(x)$ .

Figure 7 shows the rescaled magnetization data  $M/M_S$  replotted as a function of  $\mu_0 H/T$ , keeping  $M_S$  fixed at the value found at 2K. The data for  $T = 2$  K were relatively well modelled by a localized-electron, free-spin model with  $g \doteq 2$  and  $S = \frac{1}{2}$ , plotted as a green solid curve in Fig. 7. For temperatures  $15 \leq T \leq 50$  K, fits with  $S = \frac{1}{2}$  showed poor agreement with the data. Much better fits were obtained by a Brillouin function with the higher spin value  $S = \frac{3}{2}$ . As seen in the figure, for temperatures  $2 < T < 15$  K the graphs do not collapse into a single function, which is a typical signature of a free, localized spin model. Apparently, it is not possible to apply such a description for these temperatures.

## IV. DISCUSSION

The magnetization of the present carbon powder can be influenced by several factors. For example, particle shape (tube, disk, or cone), level of defects within the particles, density of magnetic impurities such as iron, and presence of gas molecules adsorbed in the sample. The contributions of these factors to the total sample magnetization  $M$  can be diamagnetic, paramagnetic, or ferromagnetic in specific temperature intervals. The amount of iron impurities and their distribution in the carbon samples are thus important attributes to evaluate due to their great impact on the magnetic properties of the samples.<sup>9,35</sup> If the size of the magnetic impurity particles is big enough, then such particles can behave ferromagnetically and give rise to a ferromagnetic contribution to the sample magnetization. Small magnetic impurities uniformly distributed in the sample can behave as non-interacting magnetic moments which show paramagnetic behavior. For example, pure iron (Fe) or magnetite ( $\text{Fe}_3\text{O}_4$ ) of impurity density level  $1 \mu\text{g/g}$  in the form of big particles can contribute to the saturation magnetization  $M_S$  amounting to  $2.2 \times 10^{-4} \text{ Am}^2\text{kg}^{-1}$  or  $1.0 \times 10^{-4} \text{ Am}^2\text{kg}^{-1}$ , respectively, at room temperature.<sup>10</sup> On the other hand, if the magnetic impurities are small and uniformly distributed their paramagnetic contribution is much smaller. Taking into account the average density of iron impurities  $60 \mu\text{g/g}$  (Sec. II B 1) and assuming that the iron particles are big enough and behave ferromagnetically, then their contribution to the saturation magnetization  $M_S$  at room temperatures is expected to be about  $13 \times 10^{-3} \text{ Am}^2\text{kg}^{-1}$  for iron impurities and  $6 \times 10^{-3} \text{ Am}^2\text{kg}^{-1}$  if they are magnetite impurities. Magnetization measurements showed a ferromagnetic contribution with saturation magnetization  $M_S = 6.3 \times 10^{-3} \text{ Am}^2\text{kg}^{-1}$  (Fig. 5), which falls inside this range of theoretical saturation values. However, ZFC and FC measurements (Fig. 3) do not show clear evidence of a blocking temperature associated with an Fe ferromagnetic phase. It is highly probable that the ferromagnetic part of the signal at all temperatures is the result of iron-containing microparticles, which could stem from the pyrolytic production process.<sup>12</sup> However, no such particles have been identified in electron microscopy images or in energy-dispersive x-ray (EDX) spectra. We conclude that in the present samples the expected contribution to the saturation magnetization  $M_S$  from magnetic iron impurities is comparable to the measured magnetization at room temperatures. However, at low temperatures  $T < 100\text{K}$  the dominating contribution to  $M_S$  comes from the carbon particles. Thus, the isothermal magnetization function  $M_{F,T=300\text{K}}$  at temperature

$T = 300$  K was subtracted from the experimental magnetization curves to correct for the ferromagnetic contribution from the magnetic impurities as explained in Sec. III C.

The total magnetization of the samples is composed of a relatively strong negative diamagnetic signal and a smaller positive magnetization. This combination is a common feature of the magnetization of HOPG samples.<sup>10,12,19</sup> It differs from the behavior for nanodiamond powders<sup>14</sup> and carbon nanofoams,<sup>13</sup> where the magnetization is dominated by the paramagnetic contribution of orbital electrons. The diamagnetic susceptibility of the carbon powder is similar to what has been observed for other carbon allotropes, for example the HOPG samples<sup>10,19</sup> and mono- and bilayer graphene crystallites of sizes 10 to 50 nm.<sup>16</sup> This common feature is explained by delocalized  $\pi$  electrons in carbon rings where currents are induced by the external magnetic field.<sup>8</sup> The magnetic susceptibility of diamond and  $C_{60}$  does not depend strongly on the temperature.<sup>8</sup> On the other hand, the diamagnetic susceptibility of a 2D honeycomb carbon lattice has been calculated to be temperature dependent with an absolute value that increases with temperature.<sup>3,8</sup> In order to simplify the separation of diamagnetic, paramagnetic, and ferromagnetic contributions we had to assume that the diamagnetic contribution is constant and independent of temperature.

For low magnetic fields [Figs. 3 (a) and (b)], the temperature dependences of ZFC and FC magnetizations are irreversible in a wide temperature range. This observation agrees with previous results showing thermal hysteresis.<sup>11,18,36,37</sup> It is often assumed that such magnetization behavior originates from isolated spin clusters<sup>11,18,36</sup> which could display a spin-glass like state.<sup>36</sup> As seen in Figs. 3 (b) and 3(c), for temperatures  $2 \leq T < 100$  K and magnetic fields  $0.1 \leq \mu_0 H \leq 4$  T, the magnetization follows a power law  $M \sim T^{-\alpha}$  with exponent  $\alpha < 1$ . The exponent  $\alpha < 1$  differs from that of nanodiamond powder,<sup>14</sup> graphene sheets,<sup>16</sup> and HOPG samples,<sup>12</sup> where a Curie law behavior,  $\alpha = 1$ , was observed for magnetic fields of 1 T. It has been found earlier that certain magnetic materials, for example doped semiconductors<sup>13</sup> or certain rare-earth intermetallics,<sup>38</sup> show exponents  $\alpha < 1$  for low temperatures and low magnetic fields. An exponent  $\alpha < 1$  indicates that there are magnetic spin interactions.<sup>38</sup> Bhatt and Lee<sup>39</sup> found an exponent  $\alpha < 1$  for a 3D model of spatially random Heisenberg spins  $S = \frac{1}{2}$  that interact through an exponentially decaying interaction vs separation. The ESR spectra in Fig. 2 show a tendency of localization of electrons when the temperature decreases ( $T < 38$  K). For the lowest temperature  $T = 2$  K, the ESR spectrum resembles the spectrum of an insulator and the magnetization vs

magnetic field is well approximated by the Brillouin model of noninteracting spins  $S = \frac{1}{2}$ . For temperatures  $2 < T < 15$  K, the magnetization is higher than that predicted by the Brillouin function-based model for  $S = \frac{1}{2}$ . However, at  $T = 15$  K it is well approximated by a Brillouin function with  $S = \frac{3}{2}$ . It is possible that both localized and itinerant magnetic processes can coexist in this temperature range, resulting in a behavior that looks like a smooth change of the apparent average spin value  $\langle S \rangle$  from  $\frac{1}{2}$  to  $\frac{3}{2}$  as temperature increases (Fig. 7). Similarly, for  $15 \leq T < 50$  K the magnetization can be consistently approximated by a Brillouin function with spin  $S = \frac{3}{2}$  (data for  $T = 20, 30,$  and  $40$  K are not shown). The magnetization vs. temperature results are similar to the results observed for carbon nanofoams.<sup>13</sup> Contrary to our observation of a changing  $S$  value, it has been found that for graphene sheets<sup>16</sup>  $S = 2$  and  $S = \frac{5}{2}$  and for graphene sheets with induced point defects<sup>12</sup>  $S = \frac{1}{2}$ , independent of temperature. One possible explanation for the differences between our results and these results could be the different structure of the graphene sheets and the present nanoparticles, which consist of a mixture of crystalline and disordered phases where each phase can contribute separately to the sample magnetization. The behavior of the spins at the interface between these phases is unknown. To clarify these points, future studies are needed of samples containing purified phases.

## V. CONCLUSION

We have measured magnetization properties of carbon powder samples containing carbon cones and disks. A ferromagnetic contribution is consistent with the known amount of Fe impurities in the sample and was identified and subtracted from the data. The measurements showed thermal hysteresis in the magnetization for weak fields which we believe is due to magnetic ordering intrinsic to the carbon particles. Based on the results of ESR spectra and magnetization vs temperature and magnetization vs magnetic field measurements, it seems that there exist localized electrons at temperature  $T = 2$  K, and their response to magnetic field is well described by a free-spin  $S = \frac{1}{2}$  model. For temperatures  $2 < T < 50$  K the magnetization is higher than that calculated from the Brillouin function for this model, which may be a result of interactions among localized- or itinerant- electron spins in this temperature range. Similar magnetic behavior has been found in other carbon-based materials like HOPG, diamond, nanofoams, and graphene sheets, but there are also clear

differences between the current material and the earlier reports on other samples. More studies are needed to learn more about the complicated interactions among localized and itinerant magnetic moments in the growing class of carbon nanomaterials.

### Acknowledgments

The authors would like to thank Jaroslav Král for valuable discussion and Jaroslav Černý for operating the Van de Graaff accelerator as well as J. P. Pinheiro of n-Tec AS for providing the samples used in this study. This work was supported by Institutional Research Plan No. MSM6840770040, by SAS Centre of Excellence CFNT MVEP, and by Research Council of Norway Grant No. 191621/F20.

- 
- <sup>1</sup> F. Hennrich, C. Chan, V. Moore, M. Rolandi, and Mike O'Connell, in *Carbon Nanotubes: Properties and Application*, edited by M. J. O'Connell (CRC / Taylor & Francis, Boca Raton, FL, 2006), Chap. 1,
  - <sup>2</sup> A. Hirsch, *Nature Mater.* **9**, 868 (2010).
  - <sup>3</sup> A. H. Castro Neto, F. Guinea, N. M. R. Peres, K. S. Novoselov, and A. K. Geim, *Rev. Mod. Phys.* **81**, 109 (2009).
  - <sup>4</sup> Xian-Lei Sheng, Qing-Bo Yan, Fei Ye, Qing-Rong Zheng, and Gang Su, *Phys. Rev. Lett.* **106**, 155703 (2011).
  - <sup>5</sup> A. Krishnan, E. Dujardin, M. M. J. Treacy, J. Hugdahl, S. Lynum, and T. W. Ebbesen, *Nature (London)* **388**, 451 (1997).
  - <sup>6</sup> S. Dimovski and Y. Gogotsi, in *Carbon Nanomaterials*, edited by Y. Gogotsi, (CRC / Taylor & Francis, Boca Raton, FL, 2006).
  - <sup>7</sup> T. L. Makarova, *Semiconductors* **38**, 641 (2004).
  - <sup>8</sup> R. C. Haddon, *Nature (London)* **378**, 249 (1995).
  - <sup>9</sup> P. Esquinazi, in *Handbook of Magnetism and Advanced Magnetic Materials, Vol 4: Novel Materials*, edited by H. Kronmüller and S. Parkin (John Wiley & Sons, New York, 2007).
  - <sup>10</sup> R. Höhne, P. Esquinazi, V. Heera, H. Weishart, A. Setzer, and D. Spemann, *J. Magn. Magn. Mater.* **320**, 966 (2008).

- <sup>11</sup> Y. Kopelevich, R. R. da Silva, J. H. S. Torres, A. Penicaud, and T. Kyotani, Phys. Rev. B **68**, 092408 (2003).
- <sup>12</sup> R. R. Nair, M. Sepioni, I-Ling Tsai, O. Lehtinen, J. Keinonen, A. V. Krasheninnikov, T. Thomson, A. K. Geim, and I. V. Grigorieva, Nat. Phys. **8**, 199 (2012).
- <sup>13</sup> A. V. Rode, E. G. Gamaly, A. G. Christy, J. G. Fitz Gerald, S. T. Hyde, R. G. Elliman, B. Luther-Davies, A. I. Veinger, J. Androulakis, and J. Giapintzakis, Phys. Rev. B **70**, 054407 (2004).
- <sup>14</sup> E. M. Levin, X. W. Fang, S. L. Bud'ko, W. E. Straszheim, R. W. McCallum, and K. Schmidt-Rohr Phys. Rev. B **77**, 054418 (2008).
- <sup>15</sup> F. Hellman, M. Q. Tran, A. E. Gebala, E. M. Wilcox, and R. C. Dynes, Phys. Rev. Lett. **77**, 4652 (1996).
- <sup>16</sup> M. Sepioni, R. R. Nair, S. Rablen, J. Narayanan, F. Tuna, R. Winpenny, A. K. Geim, and I. V. Grigorieva, Phys. Rev. Lett. **105**, 207205 (2010).
- <sup>17</sup> D. Spemann, K. H. Han, R. Höhne, T. Makarova, P. Esquinazi, and T. Butz, Nucl. Instrum. Methods Phys. Res. Sect. B **210**, 531 (2003).
- <sup>18</sup> D. W. Boukhvalov, P. F. Karimov, E. Z. Kurmaev, T. Hamilton, A. Moewes, L. D. Finkelstein, M. I. Katsnelson, V. A. Davydov, A. V. Rakhmanina, T. L. Makarova, Y. Kopelevich, S. Chiuzbaian and M. Neumann, Phys. Rev. B **69**, 115425 (2004).
- <sup>19</sup> J. Červenka, M. I. Katsnelson, and C. F. J. Flipse, Nat. Phys. **5**, 840 (2009).
- <sup>20</sup> D. Martínez-Martín, M. Jaafar, R. Pérez, J. Gómez-Herrero, and A. Asenjo, Phys. Rev. Lett. **105**, 257203 (2010).
- <sup>21</sup> J. González, F. Guinea, and M. A. H. Vozmediano, Phys. Rev. B **63**, 134421 (2001).
- <sup>22</sup> N. Park, M. Yoon, S. Berber, J. Ihm, E. Osawa, and D. Tománek, Phys. Rev. Lett. **91**, 237204 (2003).
- <sup>23</sup> O. V. Yazyev and L. Helm, Phys. Rev. B **75**, 125408 (2007).
- <sup>24</sup> P. Esquinazi, D. Spemann, R. Höhne, A. Setzer, K.-H. Han, and T. Butz, Phys. Rev. Lett. **91**, 227201 (2003).
- <sup>25</sup> Y. Shibayama, H. Sato, T. Enoki, and M. Endo, Phys. Rev. Lett. **84**, 1744 (2000).
- <sup>26</sup> J. Hughdahl, K. Hox, S. Lynum, R. Hildrum, and M. Norvik, Norwegian Patent No. PCT/NOR98/00093.
- <sup>27</sup> H. Heiberg-Andersen, G. W. Walker, A. T. Skjeltorp, and S. N. Naess, in *Handbook of Nanopf*

- ysics 5 - Functional Nanomaterials*, edited by K. D. Sattler (CRC, Boca Raton, FL, 2011), Chap. 25,.
- <sup>28</sup> T. Garberg, S. N. Naess, G. Helgesen, K. D. Knudsen, G. Kopstad, and A. Elgsaeter, *Carbon* **46**, 1535 (2008).
- <sup>29</sup> S. N. Naess, A. Elgsaeter, G. Helgesen, and K. D. Knudsen, *Sci. Technol. Adv. Mater.* **10**, 065002 (2009).
- <sup>30</sup> Y. Gogotsi, S. Dimovski, and J. A. Libera, *Carbon* **40**, 2263 (2002).
- <sup>31</sup> S. Iijima, M. Yudasaka, R. Yamada, S. Bandow, K. Suenaga, F. Kokai, K. Takahashi, *Chem Phys. Lett.* **309**, 165 (1999).
- <sup>32</sup> Sven A. E. Johansson, John L. Campbell, and Klas G. Malmqvist, *Particle-Induced X-Ray Emission Spectrometry (PIXE)*, (John Wiley & Sons, New York, 1995).
- <sup>33</sup> <http://pixe.physics.uoguelph.ca/gupix/main/>
- <sup>34</sup> H. E. Stanley, *Introduction to Phase Transitions and Critical Phenomena*, (Clarendon Press-Oxford, 1971).
- <sup>35</sup> P. Esquinazi, J. Barzola-Quiquia, D. Spemann, M. Rothermel, H. Ohldag, N. García, A. Setzer, and T. Butz, *Magn. Mater.* **322**, 1156 (2010).
- <sup>36</sup> D. Arčon, Z. Jagličič, A. Zorko, A. V. Rode, A. G. Christy, N. R. Madsen, E. G. Gamaly, and B. Luther-Davies, *Phys. Rev. B* **74**, 014438 (2006).
- <sup>37</sup> A. W. Mombrú, H. Pardo, R. Faccio, O. F. de Lima, E. R. Leite, G. Zanelatto, A. J. C. Lanfredi, C. A. Cardoso, and F. M. Araújo-Moreira, *Phys. Rev. B* **71**, 100404(R) (2005).
- <sup>38</sup> S. Ghosh, T. F. Rosenbaum, G. Aeppli, and S. N. Coppersmith, *Nature (London)* **425**, 48 (2003).
- <sup>39</sup> R. N. Bhatt and P. A. Lee, *Phys. Rev. Lett.* **48**, 344 (1982).